Kinetics and Mechanism of the CN + NCO → NCN + CO Reaction Studied by Experiment and Theory

Shiang-Yang Tzeng,[†] Po-Hsueh Chen,[†] Niann S. Wang,*[,†] L. C. Lee,[‡] Z. F. Xu,[§] and M. C. Lin*[,†,§]

Department of Applied Chemistry and Center for Interdisciplinary Molecular Science, Chiao Tung University, Taiwan 30010, Department of Electrical and Computer Engineering, San Diego State University, San Diego, California 92182, and Department of Chemistry, Emory University, Atlanta, Georgia 30322

Received: March 2, 2009; Revised Manuscript Received: April 3, 2009

The rate coefficients for the CN + NCO → NCN + CO reaction have been measured by a laser-photolysis/laser-induced fluorescence technique in the temperature range of 254−353 K and the He pressures of 123−566 Torr. The CN radical was produced from the photolysis of BrCN at 193 nm, and the NCO radical from the CN + O_2 reaction. The NCN radical was monitored by laser-induced fluorescence with a dye laser at 329.01 nm. The rate constants derived from kinetic modeling, with a negative temperature dependence but no pressure effect, can be expressed by $k = (2.15 \pm 0.70) \times 10^{-11} \exp[(155 \pm 92)/T]$ cm^3 molecule^{-1} s^{-1}, where the quoted errors are two standard deviations. The reaction mechanism and rate constant have also been theoretically predicted for the temperature range of 200−3000 K at He pressures ranging from 10^{-4} Torr to 1000 atm based on dual channel Rice−Ramsperger−Kassel−Marcus (RRKM) calculations with the potential energy surface evaluated at the G2M and CCSD(T) levels. The rate constant calculated by variational RRKM theory agrees reasonably with experimental data.

1. Introduction

The cyanonitrene (NCN) radical has been recognized as an important intermediate in combustion media, since Lin and co-workers[1,2] revealed by a computational study in 2000 that this radical can be produced by the CH + N_2 reaction. NCN has been detected in the microwave discharge of CF_4/N_2/He mixture[3] and the methane−air flame[4] by the laser-induced fluorescence (LIF) technique, and in the heating mixtures of diketene/N_2 and ethane/N_2 behind reflected shock waves by photoabsorption.[5] Recent shock tube experiments confirm that H + NCN is the dominant channel of the CH + N_2 reaction;[5] and results are in better agreement with recent calculations[6] than an earlier calculation[2] that predicted lower rates constants. The higher reaction rate results from the predicted lower heat of formation of NCN. All these studies show that NCN is indeed an important intermediate in hydrocarbon/air combustion media. It has been demonstrated that the NO fractions observed in natural gas flames agree better with prediction if NCN is included in kinetic modeling.[7,8]

Because of its importance, the reaction mechanism and kinetics of NCN have been recently actively investigated. For instance, the reaction rate constants of NCN with the combustion species, such as (C, H, CH, CH_2, CH_3, and CN),[9] O_2,[10] O (^{3}P),[11] (NO, O_2, C_2H_4 and NO_2),[12] NO,[13] and NO_2,[14] have been investigated by either experimental measurements and/or theoretical calculations. However, all these investigations are related to the consumption of NCN, but not the production, which is a subject of this report.

The production of NCN from the CN + NCO reaction has been suggested long ago by Bullock and Cooper[15] during their study on the CN + O_2 reaction. However, to the authors' knowledge, the reaction rate constant is neither experimentally measured nor theoretically predicted yet. Recognizing its importance in propellant combustion, Tsang[16] recommended the rate constant for the CN + NCO reaction to be 3×10^{-11} cm^3 molecule^{-1} s^{-1} with an uncertainty of a factor of 3. In fact, this reaction rate constant could be useful in modeling of hydrogen/cyanide oxidation, because both the CN and NCO radicals were observed in a flow reactor.[17]

The measurement on the production channel of a radical−radical reaction is a challenging task,[18] because both the concentrations and time profiles of reactants need to be accounted for, which pose difficulties. The study of radical−radical reaction becomes feasible by taking the advantage of laser technology. The CN radical can be produced by laser excitation of BrCN at 193 nm in situ in a reaction zone, and its concentration can be determined by laser intensity. NCO is produced by the reaction of CN with O_2, and its concentration can be obtained by kinetic modeling. The NCN radical produced from the CN + NCO reaction can be detected by the LIF signal; and its concentration can be determined by calibration with the LIF signal from the photolysis of NCN_3 at 193 nm, for which the NCN concentration is determined by the laser intensity. The reaction rate constant can thus be derived from simulating the time profile of the NCN radical.

The rate constant for the reaction of CN and NCO in the ground state has also been calculated with dual channel RRKM theory based on the potential energy surface (PES) derived by high levels quantum chemical calculations. The results of our calculations are compared with measured experimental data.

2. Experimental Section

2.1. Experimental Setup. The experimental setup for the measurement of reaction rate constant has been described previously.[13,19] In brief, the reaction cell is a double-walled Pyrex

* Corresponding authors. E-mail: nswang7899@gmail.com (N.S.); chemmcl@emory.edu (M.C.).
[†] Chiao Tung University.
[‡] San Diego State University.
[§] Emory University.

10.1021/jp901903n CCC: $40.75
Published on Web 05/13/2009

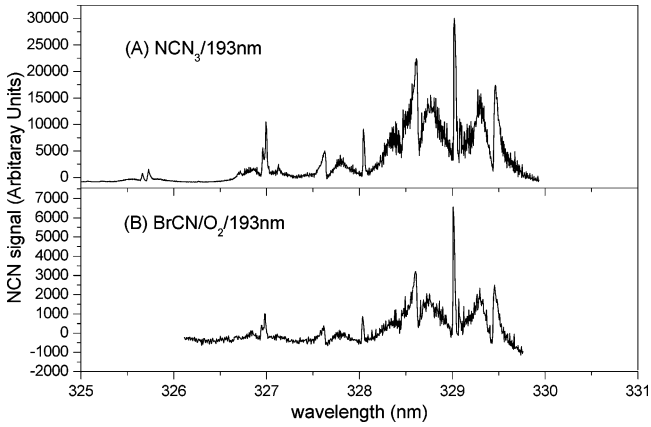

Figure 1. Excitation spectra of laser-induced-fluorescence intensities from the media: (A) NCN_3 in 100 Torr of He and (B) $BrCN/O_2$/He mixture of 122 Torr total pressure excited by ArF excimer laser at 193 nm.

flask of volume about 250 mL. The photolysis and the LIF laser beams entered and exited the cell through two pairs of mutually perpendicular baffled side arms, and intersected at the cell center. The LIF signal was projected into a photomultiplier tube mounted at a side window perpendicular to both laser beams. The LIF signal was amplified and averaged with a gated integrator. The data were stored and analyzed by a computer.

The dye laser was pumped by a doubled-output Nd:YAG laser. A delay/pulse generator was used to control the firing of both the photolysis and LIF laser beams and to initiate the boxcar integrator as well. Typically, 30−100 laser shots at a repetition rate of 5−10 Hz were averaged to obtain a single LIF data point.

The radical precursors (NCN_3, BrCN, and O_2) and the He buffer gas were mixed in a flexible tube 30 cm long before entering the reactor. The flow velocity (∼10−20 cm/s) of gas mixture was adjusted so that the reaction zone was replenished with fresh gas for each photolysis laser pulse.

The pressure of the system was measured with a Baratron gauge. The flow rates of reactants and buffer gas were measured with a calibrated mass flow meter. A temperature-controlled fluid flowed through the jacket of the reactor to maintain a constant reaction temperature (±2 K), which was measured with a K-type thermocouple placed 5 mm from the detection region. The concentrations of the reactants are determined by

$$[\mathrm{A}] = 9.66 \times 10^{18} P F_\mathrm{A}/F_\mathrm{T} T \,(\text{molecules cm}^{-3}) \qquad \text{(I)}$$

where P is the reaction pressure in Torr; T is the reaction temperature in K; F_A and F_T are the flow rates in STP cm/s (STP = 273.15 K and 760 Torr) of reactant A and the total reaction mixture, respectively. The concentration of a specific reactant was further checked via absorption of the 184.9 nmHg line with a 9.8 cm cell in the upstream of reaction cell.

He (99.999%) and O_2 (99.99%) were used without further purification. BrCN was purified in freeze−pump−thaw cycles, and diluted in He to a 2% mixture by a standard gas handling technique typically employed in experiments. NCN_3 was prepared by the reaction of NaN_3 with BrCN overnight[20] and then degassed under vacuum and diluted in He. FTIR spectrometry was used to verify purity.

2.2. LIF Signal from $BrCN/O_2$/He Excited at 193 nm. After the $BrCN/O_2$/He mixture was excited by an ArF excimer laser pulse at 193 nm, a LIF signal from the medium excited by a dye laser was observed. The excitation spectrum for the total LIF intensity is shown in Figure 1. This excitation spectrum

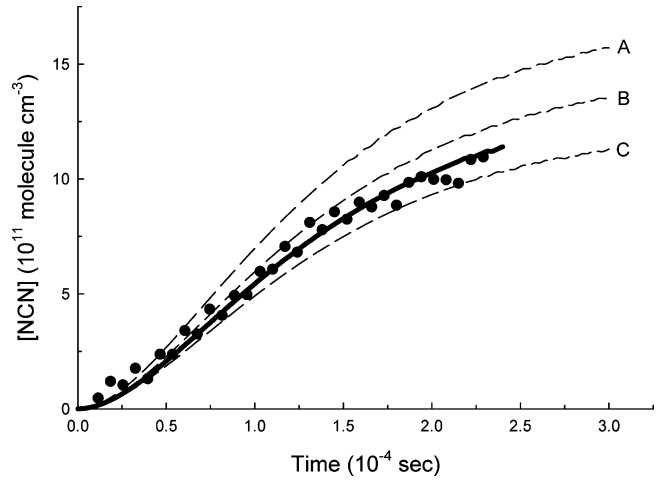

Figure 2. Temporal profiles of [NCN] at $T = 298$ K, $P = 321$ Torr, $[\mathrm{CN}]_0 = 3.73 \times 10^{13}$ molecules cm^{-3}, and $[\mathrm{O_2}]_0 = 3.07 \times 10^{14}$ molecules cm^{-3}: (●) measured data; (—) the best fit by simulation with $k_1 = 3.66 \times 10^{-11}$ cm^3 molecule^{-1} s^{-1}; (•••) simulation with the k_1 values (in 10^{-11} cm^3 molecule^{-1} s^{-1}): (A) 4.77; (B) 4.04; (C) 3.30.

of LIF is the same as that of the NCN radical observed in flame by Smith et al.[3] This result implies that NCN exists in the laser excited $BrCN/O_2$/He system.

After all possible processes are considered, NCN is most likely produced by the reaction as suggested by Bullock and Cooper[15]

$$\mathrm{CN} + \mathrm{NCO} \rightarrow \mathrm{NCN} + \mathrm{CO} \qquad (1)$$

where CN is produced by photolysis of BrCN at 193 nm

$$\mathrm{BrCN} + h\nu \rightarrow \mathrm{Br} + \mathrm{CN} \qquad \text{(II)}$$

BrCN starts to absorb photons at wavelength 260 nm as observed by Russell et al.[21] Since the absorption band is broad and smooth, the excitation at 193 nm will mainly result in dissociation so that the quantum yield for the CN production, Φ, is presumed to be equal to 1. The initial concentration of CN is determined by

$$[\mathrm{CN}]_0 = \sigma \Phi F [\mathrm{BrCN}] \qquad \text{(III)}$$

where $\sigma = 3.3 \times 10^{-19}$ cm^2 is the photoabsorption cross section at 193 nm,[21] F is the ArF excimer laser flux (photons/cm^2), and the BrCN concentration, [BrCN], was determined from eq I.

The CN radical will then react with O_2 to produce NCO by

$$\mathrm{CN} + \mathrm{O_2} \rightarrow \mathrm{NCO} + \mathrm{O} \qquad (2)$$

At 300 K, the rate constant[22−24] of this reaction is 1.73×10^{-11} cm^3 molecule^{-1} s^{-1}. The NCO radical will then react with CN to produce NCN.

2.3. Temporal Profile of [NCN] in $BrCN/O_2$/He. The LIF signal observed from the $BrCN/O_2$/He medium excited by the ArF excimer laser at 193 nm has a short induction period at the beginning, then increases with time, and saturates eventually as shown in Figure 2, where the NCN concentration, [NCN], is proportional to the LIF signal. This time profile is explainable by the presumption that the NCN radical is produced by the reaction 1, for which the production rate is

$$\mathrm{d}[\mathrm{NCN}]/\mathrm{d}t = k_1[\mathrm{CN}][\mathrm{NCO}] \qquad \text{(IV)}$$

where k_1 is the rate constant of reaction 1 which is the parameter to be measured in this study.

The CN radicals produced by the excimer laser initially carry high kinetic energy, but they will be relaxed by He buffer gas

(>125 Torr) to the equilibrium condition in a short duration (<1 μs). Since the relaxation time is much less than the measurement time scale (100 μs), [CN] can be approximated by an initial value of $[CN]_0$ at $t = 0$, and then decays exponentially with time

$$[CN] = [CN]_0 \exp(-\alpha t) \quad (V)$$

where α is the decay rate constant that contains reactions with all species in the media. In addition to reactions 1 and 2, the CN radical can be consumed by other reactions such as

$$CN + O_2 \rightarrow CO + NO \quad (3)$$

$$CN + CN + He \rightarrow NCCN + He \quad (4)$$

$$CN + O \rightarrow N + CO \quad (5)$$

$$CN + NO + He \rightarrow ONCN + He \quad (6)$$

$$CN + BrCN \rightarrow NCCN + Br \quad (7)$$

Thus, $\alpha = (k_2 + k_3)[O_2] + \gamma$, where k_2 and k_3 are the rate constants of reactions 2 and 3, and γ is the decay rate due to reactions 4−7.

The NCO radical is produced by reaction 2, its concentration can be approximated by

$$[NCO] = \eta[CN]_0(1 - \exp(-\beta t)) \quad (VI)$$

where $\beta = k_2[O_2]$ and $\eta = \beta/\alpha$.

The [NCO] can be decreased by reactions such as

$$NCO + NCO \rightarrow N_2 + 2CO \quad (8)$$

$$NCO + O_2 \rightarrow NO + CO_2 \quad (9)$$

$$NCO + O \rightarrow NO + CO \quad (10)$$

$$NCO + NO \rightarrow N_2O + 2CO \quad (11)$$

$$NCO + NO \rightarrow N_2 + 2CO \quad (12)$$

There are two reactions that are worth considering

$$CN + NCCN \rightarrow \text{products} \quad (13)$$

$$NCN + NO \rightarrow NCO + N_2 \quad (14)$$

For predicting the general feature of the temporal profile of [NCN], the reactions that involve secondary products are temporarily ignored so that α is approximately a constant. After integration with time, the NCN concentration is

$$[NCN] = a - b \exp(-\alpha t) + c \exp(-(\alpha + \beta)t) \quad (VII)$$

$$a = k_1\eta^2[CN]_0^2/(\alpha + \beta) \quad (VIII)$$

where a is the final [NCN] at long time later, $b = (1 + \eta^{-1})a$, and $c = a/\eta$.

This equation qualitatively explains the time profile shown in Figure 2, where [NCN] starts with 0 and approaches a constant value at long time later. This result implies that the presumed mechanism for the NCN production is sound; and the reaction rate constant of k_1 can be derived from the temporal profile.

It is noted that eq VII is derived only from a simplified scheme; the actual reaction mechanism needs to be studied by a sophisticated kinetic simulation. However, this equation does represent the physical picture well so that it can be used to guide the interpretation of simulation results.

2.4. Calibration of the NCN Concentration. In order to confirm the NCN detection in the $BrCN/O_2$/He system and also to calibrate its concentration, the radical was produced by photolysis of NCN_3/He with the ArF excimer laser at 193 nm under the same experimental condition (i.e., same temperature, pressure, and instrument settings).

$$NCN_3 + h\nu \rightarrow NCN + N_2 \quad (IX)$$

NCN_3 has an absorption band[25] in the range 160−200 nm. This absorption band is very broad, and excitation of NCN_3 at this band mainly dissociates into NCN + N_2.[26,27] The dissociation quantum yield is assumable to be equal to 1. The concentration of NCN_3 was determined using eq I and cross checked via absorption of the 184.9 nmHg line using the absorption cross section[25] of 5.7×10^{-18} cm^2 at this wavelength.

The excitation spectrum of the LIF signal from NCN produced by photolysis of NCN_3 is shown in Figure 1 to compare with the one produced from the $BrCN/O_2$/He system that is also shown in the figure. Both spectra are very similar, which proves the existence of NCN in the $BrCN/O_2$/He system. The similarity also indicates that the NCN radicals produced by both systems have the same rotational and vibrational populations in the ground state. The initial populations produced by the two systems are expected to be quite different; for instance, the initial NCN radicals produced from UV excitation of NCN_3/He are mainly in electronically and vibrationally excited states,[25−27] in contrast to those from $BrCN/O_2$/He that are expected to be mainly in the ground state. However, under high He buffer pressure (>125 Torr), the excited NCN radicals could be quickly relaxed to the equilibrium condition; therefore, the populations of NCN in both systems are about the same.

The same populations of NCN in both systems indicate that the LIF signal produced by the photolysis of NCN_3 can be used to calibrate the [NCN] in the $BrCN/O_2$/He system. Since the LIF signal from the transition between the ground state, X $^3\Sigma_g^-$ (0, 0^1, 0), and the excited state, A $^3\Pi_u$ (0, 2^0, 0), at 329.01 nm, is the strongest as shown in Figure 1, we select this wavelength for the detection and calibration of NCN concentration.

The NCN concentration produced by photolysis of NCN_3 at 193 nm is determined by

$$[NCN] = \sigma\Phi F[NCN_3] \quad (X)$$

where $\sigma = 3.4 \times 10^{-18}$ cm^2 is the absorption cross section of NCN_3 at 193 nm,[25] Φ (~1) is quantum yield for the NCN production, and F is the photon flux (photons/cm^2) of the ArF laser.

The LIF signal was observed to be proportional to [NCN]; thus, it can be used to determine the [NCN] in the $BrCN/O_2$/He system. Calibration procedures were carried out before, in between, and after kinetic measurements to ensure the accuracy. The error limits (2σ) for the calibrations range between 2.5 and 13.2% and for the averaged value it is ~6.5%.

2.5. Reaction Rate Constant Determined by Simulation. The typical temporal profile of [NCN] in the $BrCN/O_2$/He system shown in Figure 2 was measured at a temperature 298 K, a total pressure 321Torr, and the initial concentrations of $[CN]_0$ and $[O_2]_0$ of 3.73×10^{13} and 3.07×10^{14} molecules/cm^3, respectively. [NCN] increases from 0 to about 10^{12} molecules/cm^3 in a time duration of 230 μs.

The time profile of [NCN] is used to derive k_1 by fitting the data with simulation software Facsimile. All the 14 reactions with the rate constants[1,19,22−24,28−36] listed in Table 1 are included in the kinetic simulation. Room temperature data were employed for some of the reactions while their temperature dependence was not available. The bold line in Figure 2 is generated with a simulated k_1 of 3.66×10^{-11} cm^3 molecule^{-1} s^{-1}, which fits the data best. The simulated curves with different k_1 values of (A) 30% and (B) 10% higher as well as (C) 10% lower than the best fit value are

TABLE 1: Reaction Mechanism Used To Simulate the Rate Constant of CN + NCO

reaction	$k = A \times (T/298)^n \times e^{-(E_a/RT)}$ A (cm^3 molecule^{-1} s^{-1})	E_a (kJ/mol)	n	rate const (298 K) (cm^3 molecule^{-1} s^{-1})/ (cm^6 molecule^{-2} s^{-1})
1. CN + NCO → NCN + CO		k_1, to be determined		
2. CN + O_2 → NCO + O	1.02×10^{-11}	−1.83	−	1.73×10^{-11}[a]
3. CN + O_2 → CO + NO	1.02×10^{-11}	−1.83	−	5.52×10^{-12}[a]
4. CN + CN + He → NCCN +He	−	−	−	4.69×10^{-32}[b]
5. CN + O → N + CO	−	−	−	3.69×10^{-11}[c]
6. CN + NO + He → ONCN + He	−	−	−	2.66×10^{-30}[d]
7. CN + BrCN → NCCN + Br	2.01×10^{-11}	11.14	−	2.24×10^{-13}[e]
8. NCO + NCO → N_2 + 2CO	−	−	−	5.0×10^{-12}[f]
9. NCO + O_2 → NO + CO_2	−	−	−	5.0×10^{-17}[g]
10. NCO + O → NO + CO	−	−	−	7.0×10^{-11}[h]
11. NCO + NO → N_2O + CO	−	−	−	1.54×10^{-11}[i]
12. NCO + NO → N_2 + CO_2	1.29×10^{-10}	4.66	−1.97	1.96×10^{-11}[i]
13. NCCN + CN → products	1.05×10^{-14}	2.7	2.7	3.53×10^{-15}[j]
14. NCN + NO → NCO + N_2	−	−	−	3.0×10^{-12}[k]

[a] References 22−24. [b] Reference 28. [c] Reference 29. [d] Reference 30. [e] Reference 31. [f] Reference 32. [g] References 19 and 33. [h] References 16 and 34. [i] Reference 35. [j] Reference 36. [k] Reference 1.

TABLE 2: Summary of CN + NCO → NCN + CO Reaction Data

T (K)	P(He) (Torr)	no. of data	$[CN]_0$ (10^{13}) (molecules cm^{-3})	$[O_2]_0$ (10^{14}) (molecules cm^{-3})	k_1 (10^{-11}) (cm^3 molecule^{-1} s^{-1})[a]
254	152−564	29	0.90−2.91	1.37−6.22	4.08 ± 1.08
273	123−509	32	1.29−5.45	1.58−8.10	3.70 ± 1.46
298	123−501	44	1.78−5.15	0.81−5.89	3.51 ± 1.22
353	252−566	23	1.27−4.48	2.07−5.83	3.40 ± 1.35

[a] Error limits are 2σ.

also shown in Figure 2. For the same 10% difference, the curve (B) is more close to the best fit curve than the curve (C); that is, the fitting is less sensitive to increasing k_1 value. Nevertheless, the curve (C) is quite distinct from the best fit, indicating that the uncertainty caused by simulation is less than 5% of the best value.

At a fixed temperature, several measurements were performed at various total gas pressures and initial concentrations, $[CN]_0$ and $[O_2]_0$. The experimental conditions and results measured at four temperatures of 254, 273, 298, and 353 K are summarized in Table 2. Detailed data measured at a temperature 254 K in the He pressure range 152−564 Torr are listed in Table 3. The k_1 values of best fit are also listed in Table 3. The k_1 value averaged over 29 measurements is 4.08 ± 1.08 cm^3 molecule^{-1} s^{-1}, where the quoted errors are two standard deviations. Similarly, the detailed data measured at temperatures 273, 298, and 353 K are listed in Tables 4−6, in which the k_1 values averaged over 32, 44, and 23 measurements are 3.70 ± 1.46, 3.51 ± 1.22, 3.40 ± 1.35 cm^3 molecule^{-1} s^{-1}, respectively.

As shown in Tables 3−6, the reaction rate constants measured at each temperature are fairly constant; that is, no obvious pressure effect on k_1 is observed. This result infers that the assumption is valid that both the CN and NCN radicals are quickly relaxed to equilibrium condition. On the other hand, the averaged k_1 values decrease with temperature; that is, the reaction rate constant has a negative temperature dependence.

The Arrhenius plot for the k_1 values is shown in Figure 3; and the values can be expressed by

$$k_1 = (2.15 \pm 0.70) \times 10^{-11} \exp[(155 \pm 92)/T] \quad \text{cm}^3 \text{ molecule}^{-1} \text{ s}^{-1} \quad \text{(XI)}$$

where the quoted errors are two standard deviations.

TABLE 3: Data of NCO + CN → NCN + CO at T = 254 K and P = 152−564 Torr (He)

P (Torr)	$[CN]_0$ (10^{13}) (molecules cm^{-3})	$[O_2]_0$ (10^{14}) (molecules cm^{-3})	k (10^{-11}) (cm^3 molecule^{-1} s^{-1})
557	1.86	2.92	4.57
564	2.91	2.85	4.79
561	2.44	2.89	4.52
561	2.42	5.69	4.84
558	1.80	5.68	4.46
557	2.89	5.52	3.63
458	1.74	3.27	3.45
460	2.69	3.28	3.39
462	2.25	3.12	3.60
464	2.35	6.03	4.05
458	1.73	5.22	4.65
466	2.75	5.67	3.74
360	1.65	1.94	4.34
365	2.49	3.27	3.35
366	2.09	3.43	4.25
366	2.12	6.13	3.53
368	2.54	6.10	2.84
364	1.65	6.22	3.76
258	1.41	2.47	4.13
266	2.27	2.67	3.32
263	1.92	2.74	4.85
266	2.17	5.01	4.50
259	1.48	4.21	4.41
263	1.94	4.11	4.29
156	1.36	1.40	3.65
155	1.19	1.37	4.56
155	1.16	2.68	4.10
157	1.36	2.64	4.21
152	0.90	2.24	4.63
			av: 4.08 ± 1.08[a]

[a] Error limits are 2σ.

2.6. Discussion on Experimental Measurements. ***2.6.1. Uncertainty Related to the Branching Ratio of CN + O_2.*** All parameters that may introduce errors in k_1 shall be examined in detail to determine the accuracy of reported values. The results of sensitivity analysis on our simulation mechanism are shown in Figure 4, which indicates that the branching ratio for CN + O_2 in the reactions 2 and 3, k_2/k_3, plays a crucial role in our simulation. This importance is also foreseen in eq VIII, where k_1 is related to k_2/k_3.

The reported branching ratios of k_2/k_3 vary from 0.76/0.22[24] to 0.94/0.06.[37] The 0.76/0.22 value was employed in our simulation. If the other value of 0.94/0.06 was used, the

TABLE 4: Data of NCO + CN → NCN + CO at 273 K and P = 123−509 Torr (He)

P (Torr)	$[CN]_0$ (10^{13}) (molecules cm^{-3})	$[O_2]_0$ (10^{14}) (molecules cm^{-3})	k (10^{-11}) (cm^3 molecule^{-1} s^{-1})
506	5.45	2.65	3.08
497	2.79	2.74	4.23
502	4.35	2.70	3.56
502	4.32	6.01	3.22
509	5.32	8.10	4.46
504	2.34	4.69	3.57
395	3.44	1.77	3.79
402	5.18	3.16	3.15
403	3.46	3.34	4.33
396	1.48	2.23	5.09
403	5.34	1.58	3.23
398	3.45	2.48	4.01
400	1.43	3.00	5.03
323	4.90	5.02	4.43
327	3.82	5.15	4.95
326	3.80	2.58	4.29
320	2.65	2.73	4.29
324	4.96	2.52	3.28
247	3.18	4.96	3.36
252	1.32	2.27	4.31
248	4.83	3.49	2.78
252	3.15	3.79	3.60
245	4.86	2.08	2.70
252	3.18	2.17	3.14
247	4.83	4.90	3.24
247	1.39	5.34	3.96
123	1.34	2.23	3.14
126	4.28	4.68	2.66
126	1.29	5.48	4.74
124	2.97	2.41	2.89
125	2.91	4.78	3.43
125	2.19	4.40	2.58
			av: 3.70 ± 1.46[a]

[a] Error limits are 2σ.

simulation would give a k_1 value of 20% smaller. This shows the possible error that might be introduced to the reported k_1 value by the uncertainty of k_2/k_3.

2.6.2. Uncertainty Related to Variation of $[O_2]_0$. The higher the $[O_2]$, the faster will be the [NCN] produced so that the induction period is shortened. However, the final [NCN] will be smaller, because CN will be converted more to non-NCO products by reaction 3. This expectation is foreseen in eqs VII and VIII, where α and β increase with $[O_2]$ so that both the induction period and the final [NCN], a, decrease.

The effects of $[O_2]$ on the temporal profiles of [NCN] were investigated in detail both by measurement and simulation as shown in Figure 5. The experimental condition was set at a temperature 298 K, a pressure 250 Torr, and $[CN]_0 = 2.95 \times 10^{13}$ molecules cm^{-3}. The data were measured at $[O_2]_0$ of (1.53, 2.93, and 4.45) $\times$ 10^{14} molecules cm^{-3}; and, they were best fit by k_1 of (4.44, 4.06, and 4.27) $\times$ 10^{-11} cm^3 molecule^{-1} s^{-1}, respectively. The simulated results at higher $[O_2]_0$ of (6.0 and 20.0) $\times$ 10^{14} molecules cm^{-3} are also included in Figure 5. These results are consistent with our expectation that the induction period is shortened and the final [NCN] decreases when $[O_2]_0$ is increased. The best fit k_1 values were determined with $[O_2]_0$ varied in the range of (0.81−8.10) $\times$ 10^{14} molecules cm^{-3}, no correlation between k_1 and $[O_2]_0$ is found.

The noncorrelation between k_1 and $[O_2]_0$ indicates that the reaction kinetics used in the simulation is adequate, and no other reactions that may be important in the system are not considered. However, the possible NCN production from the reactions such as NCO + NCO and NCO + NO would expect no difference on the final [NCN] at varied $[O_2]_0$, if the $[CN]_0$ is kept at a fixed value. The effect of these possible reactions on the simulation can be examined by measuring k_1 at varied $[CN]_0$.

TABLE 5: Data of NCO + CN → NCN + CO at T = 298 K and P = 123−501 Torr (He)

P (Torr)	$[CN]_0$ (10^{13}) (molecules cm^{-3})	$[O_2]_0$ (10^{14}) (molecules cm^{-3})	k (10^{-11}) (cm^3 molecule^{-1} s^{-1})
501	5.15	5.22	3.87
497	3.91	5.40	4.92
495	3.93	3.65	3.38
500	5.12	2.41	3.07
496	2.78	2.00	3.97
321	3.73	3.07	3.66
321	2.50	3.25	4.61
321	4.68	3.00	3.14
322	4.67	5.33	3.78
324	3.61	5.89	5.00
396	2.33	5.31	3.14
401	3.39	3.05	3.45
403	3.37	5.08	2.86
398	4.38	2.88	2.99
398	4.36	4.94	2.53
245	1.92	1.53	4.15
245	1.91	2.93	4.46
246	1.86	4.45	4.64
250	2.98	1.53	4.44
250	2.95	2.93	4.06
251	2.92	4.45	4.27
255	5.12	1.53	3.49
255	5.10	2.93	3.54
256	5.07	4.45	3.84
126	1.82	0.81	2.73
126	1.80	1.30	3.11
123	1.83	1.50	3.55
126	1.84	1.83	3.32
123	1.82	2.33	3.10
124	1.78	2.48	3.84
127	1.81	4.69	3.59
127	2.49	0.81	2.99
127	2.45	1.30	3.19
128	2.27	1.83	3.24
126	2.45	2.33	3.55
126	2.76	1.50	2.95
127	2.82	2.48	3.41
128	2.85	5.69	3.33
129	2.9	0.81	2.86
129	2.87	1.30	2.59
129	2.91	1.83	3.34
130	2.92	2.33	3.11
131	4.66	1.50	3.29
132	4.46	2.48	3.01
			av: 3.51 ± 1.22[a]

[a] Error limits are 2σ.

2.6.3. Uncertainty Caused by Variation of $[CN]_0$. As shown in eq VIII, k_1 is roughly related to $[CN]_0^{-2}$; thus, the accuracy of k_1 is affected by the uncertainty of $[CN]_0$. Since $[CN]_0$ was determined according to eq III, its uncertainty included those of [BrCN], laser flux, absorption cross section, and quantum yield. We estimate the overall uncertainty on the determination of $[CN]_0$ is less than 10%. Our simulation showed that a 10% decrease of $[CN]_0$ will yield a 21% higher k_1, and vice versa. In other words, a 10% uncertainty in $[CN]_0$ will introduce that of 21% in k_1.

In our measurements, $[CN]_0$ was varied over a wide range to examine possible errors. As examples, the temporal profiles of [NCN] measured at a temperature 273 K, a He pressure 500 Torr, $[O_2]_0 = 2.74 \times 10^{14}$ molecules cm^{-3}, and $[CN]_0$ varied at

TABLE 6: Data of NCO + CN → NCN + CO at $T = 353$ K and $P = 252-566$ Torr (He)

P (Torr)	$[CN]_0$ (10^{13}) (molecules cm^{-3})	$[O_2]_0$ (10^{14}) (molecules cm^{-3})	k (10^{-11}) (cm^3 molecule^{-1} s^{-1})
560	2.09	3.06	3.74
565	2.40	3.02	3.63
566	2.43	5.83	3.65
564	2.34	4.69	4.21
493	2.30	5.13	3.39
498	3.42	2.91	3.06
504	4.48	3.58	3.21
505	4.43	4.77	4.04
493	2.32	2.87	5.02
396	2.33	5.31	3.53
401	3.39	3.05	3.88
403	3.37	5.08	3.21
398	4.38	2.88	3.36
398	4.36	4.94	2.84
319	2.38	2.88	2.36
323	2.43	5.31	2.54
323	3.45	2.70	2.55
322	3.45	5.21	2.64
251	2.93	4.65	3.06
245	3.79	2.44	3.09
252	3.75	4.39	2.73
256	1.39	2.07	4.43
252	1.27	3.31	4.09
			av: 3.40 ± 1.35[a]

[a] Error limits are 2σ.

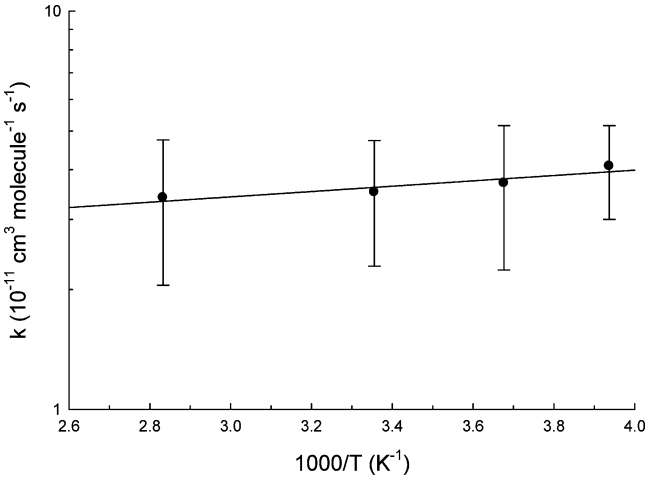

Figure 3. The Arrhenius plot of k_1.

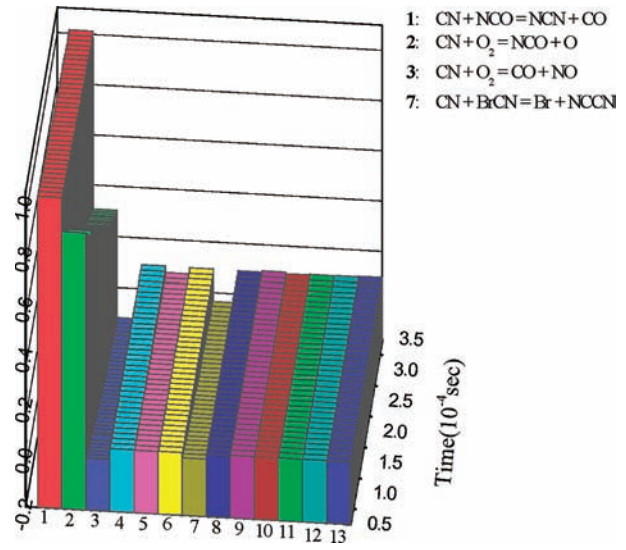

Figure 4. Sensitivity analysis at 254 K. Reaction numbers match with those in Table 1.

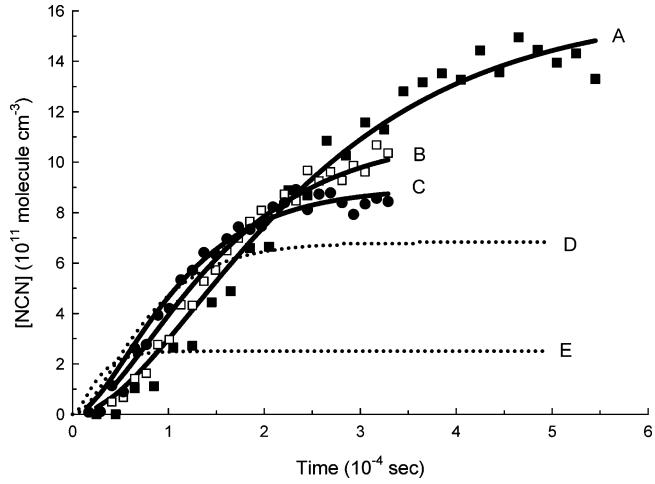

Figure 5. Temporal profiles of [NCN] at $T = 298$ K, $P = 250$ Torr, and $[CN]_0 = 2.95 \times 10^{13}$ molecules cm^{-3}. $[O_2]_0$ (in 10^{14} molecules cm^{-3}) are (A) 1.53 (■); (B) 2.93 (□); and (C) 4.45 (●). The solid lines (—) show the best fit by simulations with k_1 (in 10^{-11} cm^3 molecule^{-1} s^{-1}) of (A) 4.44; (B) 4.06; and (C) 4.27. The dotted lines (•••) show the simulated results at $[O_2]_0$ (in 10^{14} molecules cm^{-3}) of (D) 6.0 and (E) 20.0.

(2.79 and 4.35) × 10^{13} molecules cm^{-3} are shown in Figure 6, where the best fit k_1 values at varied $[CN]_0$ are (4.23 and 3.56) × 10^{-11} cm^3 molecule^{-1} s^{-1}, respectively. The simulated profiles of [NCN] at $[CN]_0$ of (7.17 and 14.3) × 10^{13} molecules cm^{-3} are also shown in Figure 6. Both the experimental data and simulated profiles show that the induction periods do not vary, but the final [NCN] increases with $[CN]_0$. These results are expected from eq VII where α and β do not depend on $[CN]_0$ so that the induction period does not vary; and, from eq VIII the final [NCN], a, increases with $[CN]_0$. Over the $[CN]_0$ range of (0.90−5.45) × 10^{13} molecules cm^{-3} studied in our measurements, no correlation between the best fit k_1 value and $[CN]_0$ is found.

These results of the noncorrelation between k_1 and $[CN]_0$, again, show that the reaction kinetics used in the simulation is adequate, and the measured k_1 values do not contain systematically errors due to some possible CN reactions being excluded from the simulation scheme. It is noted that the possibility of NCN production from CN + CN reaction is excluded in the simulation; this is in fact justified by our observation that no NCN is detected in the photolysis of BrCN/He at 193 nm.

2.6.4. Uncertainty Caused by Calibration of [NCN]. The rate constants of reaction 1 were determined by simulating the temporal profiles of [NCN]. Our simulation shows that a 10% increase of [NCN] will yield a 10% higher k_1, and vice versa. In other words, a 10% uncertainty in [NCN] will introduce that of 10% in k_1. Uncertainty on [NCN] included those of [NCN_3], laser flux, absorption cross sections, and quantum yield. We estimate the overall uncertainty on the determination of [NCN] is less than 15%.

2.6.5. Quenching of ^{1}NCN. Theoretical calculations (discussed later) showed that reaction 1 produced mainly electronically excited NCN under our experimental conditions. However, the rate constants were obtained by measuring the LIF signal of the ground triplet state on the assumption that all NCN radicals were effectively quenched to their ground state in a time scale of a few microseconds or less. The lack of correlations

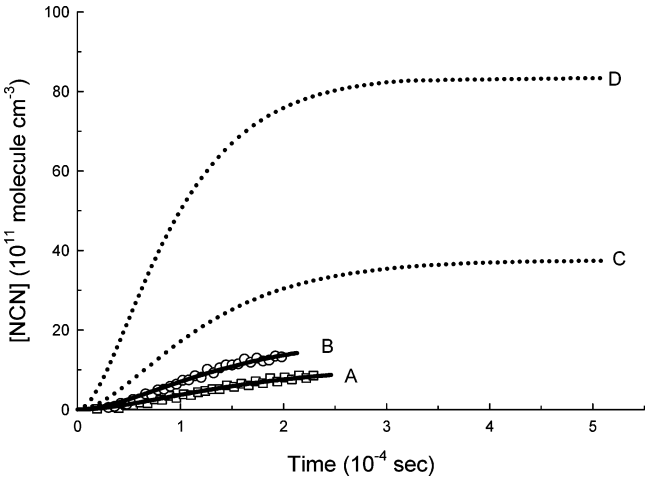

Figure 6. Temporal profiles of [NCN] at temperature 272 K, He pressure 500 Torr, $[O_2]_0 = 2.72 \times 10^{14}$ molecules cm^{-3}, and $[CN]_0$ (in 10^{13} molecules cm^{-3}) = (A) 2.79 (□) and (B) 4.35 (○). The solid lines (—) show the best fit from simulations with k_1(in 10^{-11} cm^3 molecule^{-1} s^{-1}) values of (A) 4.23 and (B) 3.56. The dotted lines (•••) show the simulated results at higher $[CN]_0$ (in 10^{13} molecules cm^{-3}): (C) 7.17 and (D) 14.3.

between the fitted k_1 and both pressure (He) and $[O_2]_0$ may clearly support this point. Further study in a bath gas of high quenching efficiency, such as Xe, would be of interest to verify the validity of our assumption.

2.6.6. Summary on Measurements. The difficulty for determining the rate constant of a radical−radical reaction cannot be overemphasized, because the procedure involves accurate measurement of radical concentration and adequate kinetic simulation. We have cautiously examined all possible error sources in the current study. The quoted errors of two standard deviations listed in Table 2 vary from 27 to 40% of the given k_1 values. The uncertainty that includes all possible errors in experiment and simulation is estimated to be not beyond 40% of the given value.

The current studied reaction rate constant has not yet been measured or calculated. The only value of 3×10^{-11} cm^3 molecule^{-1} s^{-1} estimated by Tsang[16] for the NC + NCO → NCNCO reaction coincides with our experimental value $(3.51 \pm 1.22) \times 10^{-11}$ cm^3 molecule^{-1} s^{-1} at 298 K. However, the production of NCN by the dissociation of the stabilized NCNCO molecule is unlikely because of the high dissociation energy which requires a positive temperature dependence; this contradicts the current result that the reaction has a small negative temperature dependence. The current results indicate that the NCN radical is likely produced by a barrierless association/dissociative process, as will be discussed below on the basis of the mechanism derived from ab initio MO calculations.

3. Computational Section

3.1. Computational Methods. All geometric parameters of the reactants, products, transition states, and molecular complexes of the NCO + CN reaction are optimized on the singlet and triplet potential energy surfaces at the spin-unrestricted B3LYP/6-311+G(d) level of theory.[38−41] All the stationary points were identified for local minima and transition states by vibrational analysis. Intrinsic reaction-coordinate analyses[42,43] were performed to confirm the connections of transition states with designated reactants, products, and intermediates. Based on the optimized geometries, higher level single-point energy calculations with the stationary points were performed by the G2M(CC2) method,[44] which calculated the base energy at the PMP4/6-311G(d,p) level of theory and improved with the expanded basis set and the coupled cluster method as well as "higher level corrections (HLC)". Also, for the lowest energy channels, the stationary points were optimized by the QCISD CCSD methods[45] with the 6-311+G(d) basis set and their energies were corrected by the QCISD(T) and CCSD(T) method,[45] respectively, with the 6-311+G(3df) basis set. All electronic structure calculations were performed with the Gaussian 03 program.[46]

The rate constants were calculated by the Variflex program[47] based on the microcanonical variational transition state (VTST) and Rice−Ramsperger−Kassel−Marcus (RRKM) theory.[48−50] The component rates were evaluated at the *E*/*J*-resolved level and the pressure dependence was treated by one-dimensional master equation calculations using the Boltzmann probability of the complex for the *J*-distribution. For the barrierless association/decomposition process, the fitted Morse function with the bond distance *R*(NC−NCO)was used to approximate the minimum potential energy path (MEP); the potential for the transitional modes was described in terms of three internal angles (θ_1 (∠CNC), θ_2 (∠NCN), θ_3 (∠NCNC)) with a sum of products (in pairs) of sinusoidal functions.[51] The coefficients in the transitional potential expression as functions of the bond distance R are estimated by calculating the appropriate force constant matrix related to θ_1, θ_2, and θ_3 at the singlet NCNCO complex. These force constant matrix elements (F_{ij}) are assumed to decay exponentially with the bond distance R: $F_{ij}(R) = F_{ij}(R_0) \exp[-\eta(R - R_0)]$, in which η is decay parameter and R_0 is the bond length of NC−NCO. For the collisional stabilization of the excited NCNCO intermediate, the Lennard-Jones parameters (ε/k = 201 K and σ = 4.04 Å) are taken to be those of the similar complex, NCNNO, in the NCN + NO reaction.[13] The Lennard-Jones parameters for He is taken to be ε/k = 10.0 K and σ = 2.55 Å from the literature[52] with the averaged step size of 100 cm^{-1} for energy transfer per collision.

3.2. Reaction Potential Surface. The optimized geometric parameters of the reactants, intermediates, and transition states are shown in Figure 7, while the relative potential energy diagram is drawn in Figure 8. The frequencies and moments of inertia of the reactants, intermediates, and transition states are listed in Table 7. One can see that the reaction heats of the products at the ground electronic state are −55.9 kcal/mol for NCN($^3\Sigma_g^-$) + CO, −45.5 kcal/mol for CCO($^3\Sigma^-$) + N_2, and −26.2 kcal/mol for CNN($^3\Sigma^-$) + CO at the G2M level. From the literature data in refs 53−55 ($\Delta_f H_0^o$(NCO($^2\Pi$)) = 38.0 ± 2.5 kcal/mol,[53] $\Delta_f H_0^o$(CN($^2\Sigma^+$)) = 104.4 ± 2.4 kcal/mol,[53] $\Delta_f H_0^o$(NCN($^3\Sigma_g^-$)) = 111.0 kcal/mol,[54] $\Delta_f H_0^o$(CO) = −27.2 kcal/mol,[53] $\Delta_f H_0^o$(CCO($^3\Sigma^-$)) = 91.1 ± 0.5 kcal/mol,[56] and $\Delta_f H_0^o$(CCO($^3\Sigma^-$)) = 138.3 ± 1.2 kcal/mol[56]), the reaction heats are obtained to be −58.6 ± 4.9, −51.3 ± 5.5, and −31.3 ± 6.5 kcal/mol for NCN($^3\Sigma_g^-$) + CO, CCO($^3\Sigma^-$) + N_2, and CNN($^3\Sigma^-$) + CO, respectively. Our predicted results at the G2M level are within the error range of these literature data.

3.2.1. Singlet State Reaction Channels. Two channels are considered on the singlet state potential energy surface. One is a barrierless association reaction of NCO ($^2\Pi$) + CN ($^2\Sigma^+$) to form cyanogen isocyanate, NCNCO ($^1A'$) (denoted as ^{1}NCNCO), and then to go to the dissociation products of CO+NCN ($^1\Delta_g$) (denoted as ^{1}NCN). At the G2M/B3LYP/6-31+G(d) level the ^{1}NCNCO intermediate is 114.6 and 83.9 kcal/mol lower than the reactants and the ^{1}NCN + CO products, respectively. There is no tight transtion state found by the B3LYP/6-311+G(d) method on the dissociation process. So,

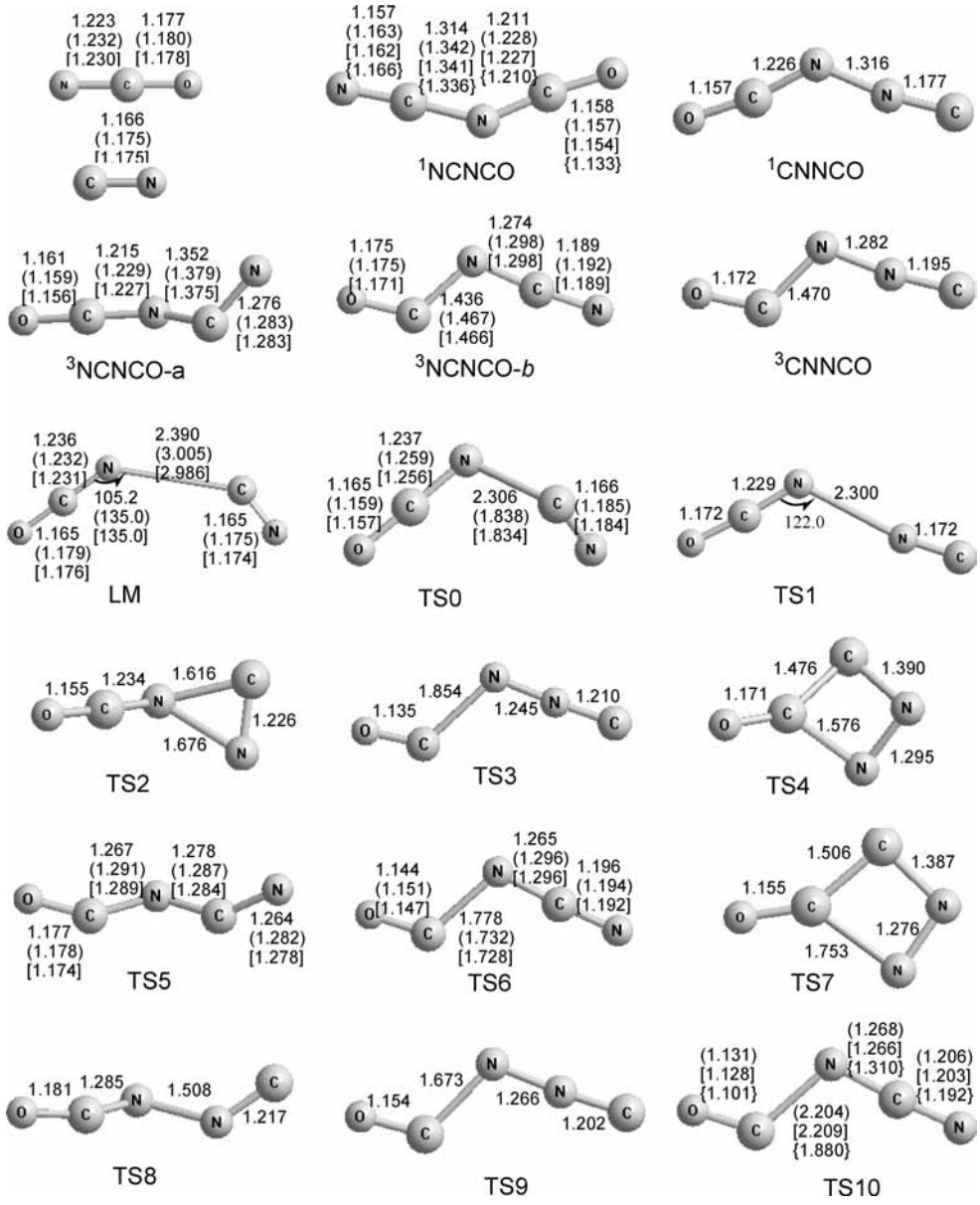

Figure 7. Geometric parameters (angstroms and degrees) of reactants, intermediates, and transition states at the B3LYP/6-311+G(d) level of theory. The numbers in parentheses, brackets, and braces are at the QCISD/6-311+G(d), CCSD/6-311+G(d), and CAS(10,10)/6-311+G(d) levels of theory, respectively.

both minimum energy paths at the G2M/B3LYP/6-31+G(d) level can be described by the Morse functions: $V_1(R) = D_e(1 - \exp[-3.745(R - 1.610)])^2$ kcal/mol for ^{1}NCNCO → NCO + CN and $V_2(R) = D_e(1 - \exp[-4.850(R - 1.314)])^2$ kcal/mol for ^{1}NCNCO → ^{1}NCN+CO. For a more reliable estimate, the minimum energy path of ^{1}NCNCO → NCO + CN was also calculated at the CASPT2(10,10)/6-311+G(d)//CAS(10,10)/6-311+G(d) level;[57,58] the result can be expressed as $V_1'(R) = D_e(1 - \exp[-4.035(R - 1.530)])^2$ kcal/mol. However, at the CAS(10,10), QCISD, and CCSD levels of theory with the 6-311+G(d) basis set, the transition state for ^{1}NCNCO → ^{1}NCN + CO, TS10, was found. It is a product-like transition state. Its C−N breaking bond is 1.880, 2.204, and 2.209 Å at the CAS(10,10), QCISD, and CCSD levels, respectively, while the corresponding imaginary frequency is *i*596, *i*228, and i232 cm^{-1}, respectively. The energies of TS10 predicted by CASPT2(10,10)/6-311+G(d)//CAS(10,10)/6-311+G(d), QCISD(T)/6-311+G(3df)//QCISD/6-311+G(d), and CCSD(T)/6-311+G(3df)//CCSD/6-311+G(d) methods are 80.1, 84.7, and 85.1 kcal/mol, respectively, higher than that of the ^{1}NCNCO intermediate, while it is 3.2, 0.4, and 0.6 kcal/mol, respectively, higher than that of ^{1}NCN + CO. It implies that the reverse reaction ^{1}NCNCO → ^{1}NCN + CO would be a low barrier process.

The second channel of the CN + NCO reaction is another association process to form cyanogen isofulminate, CNNCO (^{1}A′) (denoted as ^{1}CNNCO), via the transiton state, TS1, with a potential barrier of 5.6 kcal/mol at the G2M level. At TS1, the N−N forming bond length is 2.300 Å and the imaginary frequency is *i*215 cm^{-1} at the B3LYP/6-311+G(d) level. It is a reactant-like transition state. The energy of the ^{1}CNNCO imtermediate is −65.1 kcal/mol relative to that of the reactants, which is 49.5 kcal/mol higher than ^{1}NCNCO. The isomerization transition state, TS2, connects ^{1}CNNCO and ^{1}NCNCO with the forward barrier of 30.5 kcal/mol and the reverse barrier of 80.0 kcal/mol. Also, the ^{1}CNNCO intermediate can decompose to give CO + CNN ($^1\Delta$) (denoted as ^{1}CNN) and N_2 + CCO ($^1\Delta$) (denoted as ^{1}CCO) via TS3 and TS4, respectively. The energies of TS3 and TS4 relative to reactants are almost same; the former

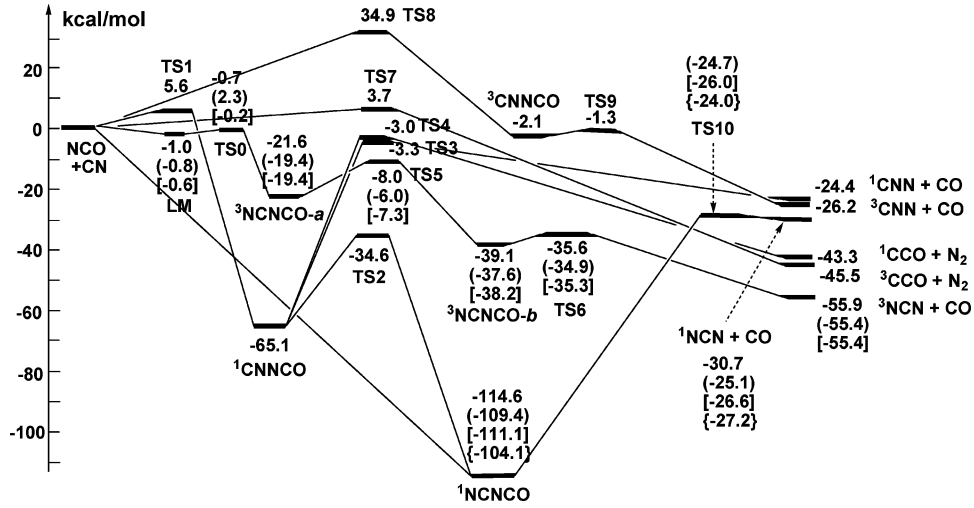

Figure 8. Potential energy surfaces of the NCO + CN reaction at the G2M//B3LYP/6-311+G(d) level of theory. The numbers in parentheses, brackets, and braces are at the QCISD(T)/6-311+G(3df)//QCISD/6-311+G(d), CCSD(T)/6-311+G(3df)//CCSD/6-311+G(d), and CASPT2(10,10)/6-311+G(d)//CAS(10,10)/6-311+G(d) levels of theory, reaspectively.

TABLE 7: Frequencies and Moments of Inertia of Reactants, Intermediates, and Transition States at the B3LYP/6-311+G(d) level of Theory[a]

species	I_a, I_b, I_c (au)	frequencies (cm^{-1})
NCO ($^2\Pi$)	150.3, 150.3	440, 440, 1272, 1563
	(155.2, 155.2)	(544, 573, 1278, 1968)
	[154.6, 154.6]	[501, 572, 1293, 1962]
	(156.2, 156.2)	(523, 563, 1260, 1970)
CN ($^2\Sigma^+$)	31.3, 31.3	2146
	(31.8, 31.8)	(2149)
	[31.8, 31.8]	[2130]
	(31.1, 31.1)	(2190)
^{1}NCNCO (^{1}A′)	16.4, 695.5, 712.0	118, 472, 491, 571, 605, 863, 1543, 2356, 2421
	(30.3, 658.6, 689.0)	(166, 453, 485, 589, 657, 894, 1480, 2336, 2378)
	[30.3, 657.0, 687.3]	[166, 474, 487, 605, 662, 898, 1495, 2359, 2397]
	(30.3, 658.6, 689.0)	(131,465, 480, 593, 663, 936, 1567, 2350, 2511)
^{3}NCNCO-*a* (^{3}A)	24.2, 680.9, 689.1	76, 174, 487, 550, 591, 897, 1479, 1615, 2344
	(34.6, 653.5, 663.9)	(144, 334, 521, 596, 653, 959, 1466, 1764, 2309)
	[32.5, 658.1, 666.6]	[144, 333, 522, 605, 656, 970, 1488, 1766, 2340]
^{3}NCNCO-*b* (^{3}A)	25.5, 668.4, 690.7	30, 189, 439, 532, 570, 802, 1232, 1819, 1949
	(29.1, 666.6, 695.7)	(153, 197, 455, 519, 555, 835, 1163, 1870, 1934)
	[29.1, 664.6, 693.8]	[151, 199, 459, 521, 557, 836, 1164, 1889, 1953]
^{1}CNNCO (^{1}A′)	24.8, 634.6, 659.4	148, 297, 344, 547, 646, 875, 1452, 2198, 2342
^{3}CNNCO (^{3}A″)	27.9, 629.3, 657.3	114, 182, 327, 449, 494, 751, 1122, 1868, 1985
LM (^{3}A)	117.8, 740.4, 850.9	8, 35, 96, 162, 493, 581, 1271, 1982, 2144
	(75.6, 1219.6, 1295.2)	(*i*42, 47, 81, 158, 555, 572, 1286, 1995, 2142)
	[75.2, 1209.7, 1284.9]	[40, 78, 157, 178, 559, 585, 1295, 1960, 2126]
TS0 (^{3}A)	123.8, 687.4, 811.3	*i*53, 44, 105, 185, 491, 580, 1267, 1985, 2138
	(97.7, 585.0, 660.3)	(*i*541, 118, 198, 438, 575, 603, 1202, 2069, 2497)
	[96.3, 583.4, 655.6]	[*i*473, 119, 198, 410, 573, 604, 1220, 1981, 2131]
TS1 (^{1}A′)	53.6, 921.2, 974.8	*i*215, 9, 41, 152, 552, 561, 1281, 2023, 2088
TS2 (^{1}A)	59.7, 502.5, 523.6	*i*264, 147, 166, 576, 604, 649, 1334, 1788, 2280
TS3 (^{1}A′)	38.3, 725.3, 763.6	*i*628, 67, 156, 285, 414, 456, 1165, 1776, 2120
TS4 (^{1}A)	94.4, 326.4, 398.4	*i*638, 311, 457, 708, 730, 935, 1010, 1375, 1970
TS5 (^{3}A)	15.8, 711.1, 715.8	*i*1197, 129, 279, 446, 530, 915, 1147, 1776, 2059
	(23.3, 698.4, 707.3)	(*i*1671, 162, 413, 472, 549, 907, 1046, 1778, 2028)
	[23.1, 696.4, 705.6]	[*i*1801, 158, 407, 465, 549, 916, 1050, 1803, 2068]
TS6 (^{3}A)	38.0, 722.2, 760.3	*i*452, 61, 163, 420, 447, 576, 1190, 1798, 2048
	(41.0, 704.4, 745.5)	(*i*547, 140, 178, 448, 457, 570, 1098, 1851, 2015)
	[41.0, 701.5, 742.5]	[*i*538, 141, 179, 452, 460, 572, 1099, 1846, 2054]
TS7 (^{3}A″)	94.8, 352.4, 447.2	*i*360, 234, 404, 641, 711, 812, 919, 1338, 2022
TS8 (^{3}A)	36.1, 648.9, 665.6	*i*1321, 97, 285, 382, 387, 533, 965, 1674, 1942
TS9 (^{3}A″)	36.2, 657.0, 693.2	*i*436, 95, 174, 349, 420, 566, 1124, 1868, 1993
TS10 (^{1}A′)	(59.4, 854.9, 914.3)	(*i*228, 189, 213, 291, 502, 546, 1200, 1815, 2199)
	[60.1, 852.2, 912.4]	[*i*232, 189, 214, 290, 490, 539, 1205, 1835, 2242]
	(54.4, 757.3, 811.8)	(*i*596, 113, 128, 275, 506, 563, 1095, 1980, 2455)

[a] The numbers in parentheses, brackets, and braces are at the QCISD/6-311+G(d), CCSD/6-311+G(d), and CAS(10,10)/6-311+G(d) levels of theory, respectively.

is −3.3 kcal/mol and the latter is −3.0 kcal/mol. They are higher than TS2 by 31 kcal/mol. This means that the isomerization subchannel from the ^{1}CNNCO intermediate is more favorable than its direct decomposition channels.

Also, the association process to singlet NCOCN was examined at both B3LYP/6-311+G(d) and CCSD/6-311+G(d) levels of theory. A transition state was found to be −0.1 and 4.5 kcal/mol relative to the reactants of NCO + NC with the former and the latter methods, respectively. Corrected by CCSD(T)/6-311+G(3df) based on the geometric parameters optimized at the CCSD/6-311+G(d) level, the transition state is 1.9 kcal/mol over the reactants. The continuing reaction following the formation of singlet NCOCN is back to the reactants NC + NCO or possibly decomposing to NCN + CO. However, the production of the latter is very difficult to take place because it involves breaking one of the triple CN bonds. Thus, comparing with the barrierless association process to singlet NCNCO, this reaction channel is expected to be negligible, although the singlet NCOCN is predicted to lie below the reactants by 68.6 kcal/mol at the CCSD(T)/6-311+G(3df)//CCSD/6-311+G(d) level.

3.2.2. Triplet State Reaction Channels. The reaction of NCO ($^2\Pi$) + CN ($^2\Sigma^+$) on the triplet state potential energy surface includes three product channels. The first one generates triplet electronic state cyanoinidogen NCN ($^3\Sigma_g^-$) (denoted as ^{3}NCN) and CO through a multiwell reaction channel, as seen in Figure 8. In this channel, the complex LM is first formed barrierlessly and its relative energy is only −1.0 kcal/mol at the G2M level. This barrierless process can be effectively expressed by the Morse function $V_3(R) = D_e(1 - \exp[-2.083(R - 2.400)])^2$ kcal/mol. Following LM, one of the triplet cyanogen isocyanate isomers (denoted as ^{3}NCNCO-*a*) is formed via the transition state, TS0, with the relative energy of −0.7 kcal/mol at the G2M levels. Because the C−N forming bond at TS0 is predicted to have a longer distance of 2.306 Å at the B3LYP/6-311+G(d) level, TS0 has a small imaginary frequency of *i*53 cm^{-1}. It is necessary to confirm its existence by optimization with a higher level of theory. By both QCISD and CCSD methods with the 6-311+G(d) basis set, the C−N forming bond lengths are predicted to be 1.838 and 1.834 Å, respectively, and the imaginary frequencies increase to *i*541 and *i*474 cm^{-1}, respectively, while the energies of TS0 are 2.3 and −0.6 kcal/mol at the QCISD(T) and CCSD(T) levels, respectively. Next, ^{3}NCNCO-*a* isomerizes to ^{3}NCNCO-*b* with the conformation changed via the transition state TS5, which is lower than reactants by 8.0, 6.0, and 7.5 kcal/mol at the G2M, QCISD(T), and CCSD(T) levels, respectively. The final step from ^{3}NCNCO-*b* to ^{3}NCN) + CO needs to overcome a small barrier of only 3.5 kcal/mol at the G2M level, 2.7 kcal/mol at the QCISD(T) level, and 2.9 kcal/mol at the CCSD(T) level.

The second triplet channel undergoes by a four-membered ring transition state, TS7, to generate N_2 and CCO ($^3\Sigma^-$) (denoted as ^{3}CCO). At the G2M level, TS7 is 3.7 kcal/mol higher than reactants and, at the B3LYP/6-311+G(d) level, its imaginary frequency is *i*360 cm^{-1}. The third channel has the highest transition state, TS8, which is 34.9 kcal/mol above the reactants at the G2M level. By TS8, the reaction proceeds to the triplet cyanogen isofulminate, CNNCO (^{3}A″) (denoted as ^{3}CNNCO), which is −2.1 kcal/mol relative to the reactants. It is obvious that ^{3}CNNCO is unstable and can decompose to CO and CNN ($^3\Sigma^-$) (denoted as ^{3}CNN) via TS9 with a small barrier of 0.8 kcal/mol at the G2M level.

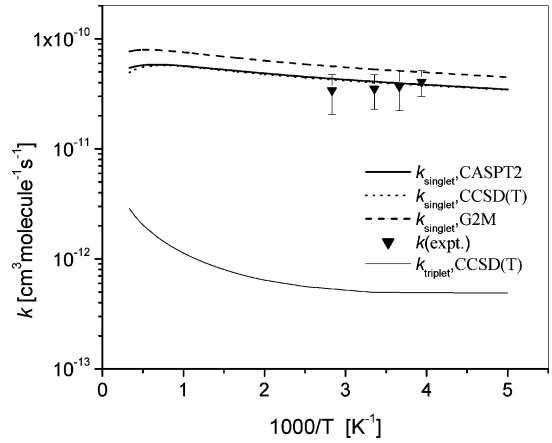

Figure 9. Predicted rate constants as a function of temperature and comparison with experimental data: (---) based on the parameters by G2M//B3LYP/6-311+G(d); (—) based on the parameters by CCSD(T)/6-311+G(3df)//CCSD/6-311+G(d).

3.3. Rate Constant Prediction and Comparison with Experiment. Based on the lowest energy reaction channels

$$NCO(^2\Pi) + CN(^2\Sigma^+) \rightarrow {}^1NCNCO \rightarrow {}^1NCN + CO \quad (15)$$

$$NCO(^2\Pi) + CN(^2\Sigma^+) \rightarrow LM \rightarrow {}^3NCNCO\text{-}a \rightarrow {}^3NCNCO\text{-}b \rightarrow {}^3NCN + CO \quad (16)$$

the rate constants are predicted using variational TST and RRKM rate theory in the temperature range from 200 to 3000 K at He pressures ranging from 10^{-4} Torr to 10^4 atm. These two product channels have been discussed above at three levels of theory: G2M//B3LYP/6-311+G(d), QCISD(T)/6-311+G(3df)//QCISD/6-311+G(d), CCSD(T)/6-311+G(3df)//CCSD/6-311+G(d), as well as CASPT2(10,10)/6-311+G(d)//CAS(10,10)/6-311+G(d). The tight transition state, TS10, was found by the latter three methods, but not by the first. The rate constants will be calculated separately by employing the energetic and geometric parameters obtained at the G2M//B3LYP/6-311+G(d), CCSD(T)/6-311+G(3df)//CCSD/6-311+G(d), and CASPT2(10,10)/6-311+G(d)//CAS(10,10)/6-311+G(d) levels.

Figure 9 shows the results of calculations using the Variflex code based on the association Morse potential and transitional potential for NCO + CN → ^{1}NCNCO with different exit transition states: the variational transition state predicted by the G2M//B3LYP/6-311+G(d) and TS10 by CCSD(T)/6-311+G(3df)//CCSD/6-311+G(d) and CASPT2(10,10)/6-311+G(d)//CAS-(10,10)/6-311+G(d). Also, in this figure the predicted rate constants are compared with the experimental data. The thicker curves, including solid, dashed, and dotted lines, represent the rate constants of the singlet reaction channel predicted with the parameters at the CASPT2(10,10)/6-311+G(d)//CAS(10,10)/6-311+G(d), CCSD(T)/6-311+G(3df)//CCSD/6-311+G(d), and G2M//B3LYP/6-311+G(d) levels, respectively. The thinner curve is the rate constant forming the triplet ^{3}NCN + CO products from the triplet reaction channel predicted by CCSD(T)/6-311+G(3df)//CCSD/6-311+G(d). Because $k_{triplet}$ is much less than $k_{singlet}$ by a factor of 20−80, the contribution of the triplet channel to the NCO + CN reaction is negligible.

From Figure 9, it can be seen that $k_{singlet}$(CASPT2) and $k_{singlet}$(CCSD(T)) are almost identical and slightly less than $k_{singlet}$(G2M). These three predicted rate constants exhibit a small positive temperature dependence because of the barrierless

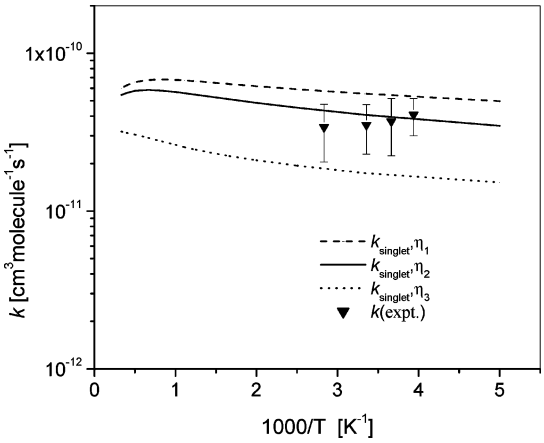

Figure 10. Comparison of predicted rate constants ($k_{singlet}$, CASPT2) at different decay parameters of force constants for transitional modes: $\eta_1 = (1.87, 3.49, 3.32)$, $\eta_2 = (1.43, 3.49, 2.32)$, $\eta_3 = (1.87, 1.85, 1.79)$.

association and the exothermic product formation with the small exit TS10 (by both CASPT2 and CCSD(T) methods) or VTS (by the G2M method). Although the experimental data display a weak negative temperature dependence that is different from calculated results, the $k_{singlet}$(CASPT2) values are in good agreement with experimental k(expt) in the experimental temperature range of 254−353 K in the error fields of the experimental data. For the major singlet product channel, the rate constant predicted by the CASPT2 and CCSD(T) methods that have an intrinsic exit barrier clearly agrees better with experimental data. The presence of TS10 restricts the exit flux and thus leads to a smaller value of rate constant.

For kinetic modeling applications, the predicted values are fitted to the expressions in units of cm^3 molecule^{-1} s^{-1}:

$$k = 2.14 \times 10^{-11} T^{0.155} \exp(-65/T) \qquad (200-1000\ \text{K})$$
$$= 7.41 \times 10^{-10} T^{0.30} \exp(-479/T) \qquad (1000-3000\ \text{K})$$

It is worth mentioning that, in the above rate constant calculation, the decay parameters (η) of the transition potential are 1.43, 3.49, and 2.32 Å^{-1}, which are obtained by the three-dimensional force constant matrix of θ_1, θ_2, and θ_3 at R_0 and R = 3.0 Å. Because the rate constant is sensitive to the decay parameters, we compared $k_{singlet}$(CASPT2) obtained at three group decay parameters, $\eta_1 = (1.87, 3.49, 3.32)$, $\eta_2 = (1.43, 3.49, 2.32)$, and $\eta_3 = (1.87, 1.85, 1.79)$ in the variational transition state range of R = 2.5−3.5 Å. The result, as drawn in Figure 10, shows that the rate constants calculated using η_1 and η_3 are respectively greater and less than the experimental data. However, the predicted rate constants by η_2 are in good agreement with the experimental values. Accordingly, η_2 can give a closer presentation of rate constant for the singlet reaction channel.

Figure 11 shows the pressure effect at three temperatures for the rate constant of NCN production via the singlet reaction channel. At 300 K, the rate constant is predicted to be independent of pressure below 1500 Torr. However, the rate constant steeply goes down with increasing pressure due to the collisional deactivation of the excited NCNCO, resulting in the decrease in the NCN + CO products. As indicated in this figure, the turning points are about 5, 50, and 500 atm at the temperatures of 300, 500, and 1000 K, respectively. At every temperature, the predicted reaction rate constants are independent of pressure below 1 atm. This is consistent with our experimental observations.

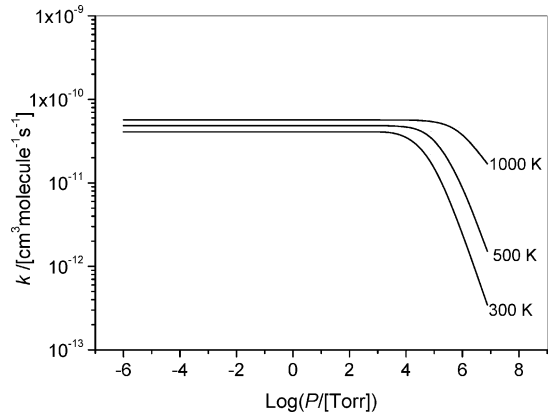

Figure 11. Predicted rate constants as a function of pressure for reaction 1.

4. Concluding Remarks

Kinetics and mechanism for the CN + NCO → NCN + CO reaction have been investigated experimentally and computationally. In our measured temperature range of 254−353 K, the reaction was found to be negatively dependent on temperature, but not on pressure in the range of 123−566 Torr. The observed pressure effect can be reasonably accounted for by the dual-channel RRKM calculations. However, the temperature effect observed by experiment is not consistent with calculations that show slightly positive temperature dependence. We have exerted a substantial effort trying to resolve this discrepancy. The possible experimental errors have been examined in great detail, and the calculations have been extended to very expensive levels. Nevertheless, a noticeable discrepancy at higher temperatures remains. Since the study of a radical−radical reaction is a challenging task in both experiment and computation, further investigation to resolve this discrepancy is of interest.

Acknowledgment. Two of us, L.C.L. and M.C.L., want to acknowledge the National Science Council of Taiwan for support of their visiting professorships at Taiwan National Chiao Tung University. Z.F.X. is grateful for partial support from the US Office of Naval Research under the grant No. N00014- 02-1-0133. S.Y.T., P.H.C., and N.S.W. thank the National Science Council of Taiwan (Contract No. NSC 95-2113-M-009-028) for support.

References and Notes

(1) Moskaleva, L. V.; Xia, W. S.; Lin, M. C. *Chem. Phys. Lett.* **2000**, *331*, 269.
(2) Moskaleva, L. V.; Lin, M. C. *Proc. Combust. Inst.* **2000**, *28*, 2393.
(3) Smith, G. P.; Copeland, R. A.; Crosley, D. R. *J. Chem. Phys.* **1989**, *91*, 1987.
(4) Smith, G. P. *Chem. Phys. Lett.* **2003**, *367*, 541.
(5) Vasudevan, V.; Hanson, R. K.; Bowman, C. T.; Golden, D. M.; Davidson, D. F. *J. Phys. Chem. A* **2007**, *111*, 11818.
(6) Harding, L. B.; Klippenstein, S. J.; Miller, J. A. *J. Phys. Chem. A* **2008**, *112*, 522.
(7) El bakali, A.; Pillier, L.; Desgroux, P.; Lefort, B.; Gasnot, L.; Pauwels, J. F.; da Costa, I. *Fuel* **2006**, *85*, 896.
(8) Lamoureux, N.; El bakali, A.; Gasnot, L.; Pauwels, J. F.; Desgroux, P. *Combust. Flame* **2008**, *153*, 186.
(9) Moskaleva, L. V. Ph.D. Dissertation, Emory University, 2001.
(10) Zhu, R. S.; Lin, M. C. *Int. J. Chem. Kinet.* **2005**, *37*, 593.
(11) Zhu, R. S.; Lin, M. C. *J. Phys. Chem. A* **2007**, *111*, 6766.
(12) Baren, R. E.; Hershberger, J. F. *J. Phys. Chem. A* **2002**, *106*, 11093.
(13) Huang, C. L.; Tseng, S. Y.; Wang, T. Y.; Wang, N. S.; Xu, Z. F.; Lin, M. C. *J. Chem. Phys.* **2005**, *122*, 184321.
(14) Yang, T. J.; Wang, N. S.; Lee, L. C.; Xu, Z. F.; Lin, M. C. *J. Phys. Chem. A* **2008**, *112*, 10185.
(15) Bullock, G. E.; Cooper, R. *J. Chem. Soc., Faraday Trans.* **1972**, *27*, 2175.

(16) Tsang, W. *J. Phys. Chem. Ref. Data* **1992**, *21*, 753.
(17) Glarborg, P.; Miller, J. A. *Combust. Flame* **1994**, *99*, 475.
(18) Pilling, M. J.; Stocker, D. W. *Annu. Rep. Prog. Chem., Sect. C* **1999**, *95*, 277.
(19) You, Y. Y.; Wang, N. S. *J. Chin. Chem. Soc.(Taipei)* **1993**, *40*, 337.
(20) Milligan, D. E.; Jacox, M. E.; Bass, A. M. *J. Chem. Phys.* **1965**, *43*, 3149.
(21) Russell, J. A.; McLaren, I. A.; Jackson, W. M.; Halpern, J. B. *J. Phys. Chem.* **1987**, *91*, 3248.
(22) Sims, I. R.; Queffelec, J. L.; Defrance, A.; Rebrion-Rowe, C.; Travers, D.; Bocherel, P.; Smith, I. W. M. *J. Chem. Phys.* **1994**, *100*, 4229.
(23) Rim, K. T.; Hershberger, J. F. *J. Phys. Chem. A* **1999**, *103*, 3721.
(24) Balla, R. J.; Casleton, K. H. *J. Phys. Chem.* **1991**, *95*, 2344.
(25) Okabe, H.; Mele, A. *J. Chem. Phys.* **1969**, *51*, 2100.
(26) Kroto, H. W. *J. Chem. Phys.* **1966**, *44*, 831.
(27) Pontrelli, G. J.; Anastassiou, A. G. *J. Chem. Phys.* **1965**, *42*, 3735.
(28) Basco, N.; Nicholas, J. E.; Norrish, R. G. W.; Vickers, W. H. J. *Proc. R. Soc. London* **1963**, *272*, 147.
(29) Titarchuk, T. A.; Halpern, J. B. *Chem. Phys. Lett.* **1995**, *232*, 192.
(30) Sims, I. R.; Smith, I. W. M. *J. Chem. Soc., Faraday Trans.* **1993**, *89*, 1.
(31) Zabarnick, S.; Lin, M. C. *Chem. Phys.* **1989**, *134*, 185.
(32) Wategaonkar, S.; Seter, D. W. *J. Phys. Chem.* **1993**, *97*, 10028.
(33) Schacke, H.; Schmatjko, K.; Wolfrum, J. *Arch. Procesow Spalania* **1974**, 5.
(34) Becker, K. H.; Kurtenbach, R.; Schmit, F.; Wisen, P. *Combust. Flame* **2000**, *120*, 570.
(35) Lin, M. C.; He, Y.; Melius, C. F. *J. Phys. Chem.* **1993**, *97*, 9124.
(36) Yang, D. L.; Yu, T.; Lin, M. C.; Melius, C. F. *J. Chem. Phys.* **1992**, *97*, 222.
(37) Schmatjko, K. J.; Wolfrum, J. *J. Ber. Bunsen-Ges. Phys. Chem.* **1978**, *82*, 419.
(38) Becke, A. D. *J. Chem. Phys.* **1993**, *98*, 5648.
(39) Becke, A. D. *J. Chem. Phys.* **1992**, *96*, 2155.
(40) Becke, A. D. *J. Chem. Phys.* **1992**, *97*, 9173.
(41) Lee, C.; Yang, W.; Parr, R. G. *Phys. Rev.* **1988**, *37B*, 785.
(42) Gonzalez, C.; Schlegel, H. B. *J. Chem. Phys.* **1989**, *90*, 2154.
(43) Gonzalez, C.; Schlegel, H. B. *J. Chem. Phys.* **1990**, *94*, 5523.
(44) Mebel, A. M.; Morokuma, K.; Lin, M. C. *J. Chem. Phys.* **1995**, *103*, 7414.
(45) Pople, J. A.; Head-Gordon, M.; Raghavachari, K. *J. Chem. Phys.* **1987**, *87*, 5968. Scuseria, G. E.; Schaefer, H. F., III. *J. Chem. Phys.* **1989**, *90*, 3700.
(46) Frisch, M. J.; Trucks, G. W.; Schlegel, H. B.; Scuseria, G. E.; Robb, M. A.; Cheeseman, J. R.; Montgomery, Jr. J. A.; Kudin, K. N.; Burant, J. C.; Millam, J. M.; Iyengar, S. S.; Tomasi, J.; Barone, V.; Mennucci, B.; Cossi, M.; Scalmani, G.; Rega, N.; Petersson, G. A.; Nakatsuji, H.; Hada, M.; Ehara, M.; Toyota, K.; Fukuda, R.; Hasegawa, J.; Ishida, M.; Nakajima, T.; Honda, Y.; Kitao, O.; Nakai, H.; Klene, M.; Li, X.; Knox, J. E.; Hratchian, H. P.; Cross, J. B.; Adamo, C.; Jaramillo, J.; Gomperts, R.; Stratmann, R. E.; Yazyev, O.; Austin, A. J.; Cammi, R.; Pomelli, C.; Ochterski, J. W.; Ayala, P. Y.; Morokuma, K.; Voth, G. A.; Salvador, P.; Dannenberg, J. J.; Zakrzewski, V. G.; Dapprich, S.; Daniels, A. D.; Strain, M. C.; Farkas, O.; Malick, D. K.; Rabuck, A. D.; Raghavachari, K.; Foresman, J. B.; Ortiz, J. V.; Cui, Q.; Baboul, A. G.; Clifford, S.; Cioslowski, J.; Stefanov, B. B.; Liu, G.; Liashenko, A.; Piskorz, P.; Komaromi, I.; Martin, R. L.; Fox, D. J.; Keith, T.; Al-Laham, M. A.; Peng, C. Y.; Nanayakkara, A.; Challacombe, M.; Gill, P. M. W.; Johnson, B.; Chen, W.; Wong, M. W.; Gonzalez, C.; Pople, J. A. *Gaussian 03, Revision C.01*; Gaussian, Inc.: Wallingford, CT, 2004.
(47) Klippenstein, S. J.; Wagner, A. F.; Dunbar, R. C.; Wardlaw, D. M.; Robertson, S. H. Variflex Version 1.00, 1999.
(48) Wardlaw, D. M.; Marcus, R. A. *Chem. Phys. Lett.* **1984**, *110*–230.
(49) Wardlaw, D. M.; Marcus, R. A. *J. Chem. Phys.* **1985**, *83*, 3462.
(50) (a) Klippenstein, S. J. *J. Chem. Phys.* **1992**, *96*, 367. (b) Klippenstein, S. J.; Marcus, R. A. *J. Chem. Phys.* **1987**, *87*, 3410.
(51) Miller, J. A.; Klippenstein, S. J. *J. Phys. Chem. A* **2000**, *104*, 2061.
(52) Hippler, H.; Troe, J.; Wendelken, H. J. *J. Chem. Phys.* **1983**, *78*, 6709.
(53) Chase, M. W., Jr. NIST-JANAF Themochemical Tables, Fourth Edition. *J. Phys. Chem. Ref. Data* **1998**, *Monograph 9*, 1.
(54) Moskaleva, L. V.; Xia, W. S.; Lin, M. C. *Chem. Phys. Lett.* **2000**, *331*, 269.
(55) Choi, H.; Mordaunt, D. H.; Bise, R. T.; Taylor, T. R.; Neumark, D. M. *J. Chem. Phys.* **1998**, *108*, 4070.
(56) Moskaleva, L. V.; Lin, M. C. *J. Phys. Chem. A* **2001**, *105*, 4156.
(57) Celani, P.; Werner, H.-J. *J. Chem. Phys.* **2000**, *112*, 5546.
(58) MOLPRO, version 2006. 1, a package of ab initio programs designed by: Werner, H.-J.; Knowles, P. J.; Lindh, R.; Manby, F. R.; Schütz, M.; Celani, P.; Korona, T.; Rauhut, G.; Amos, R. D.; Bernhardsson, A.; Berning, A.; Cooper, D. L.; Deegan, M. J. O.; Dobbyn, A. J.; Eckert, F.; Hampel, C.; Hetzer, G.; Lloyd, A. W.; McNicholas, S. J.; Meyer, W.; Mura, M. E.; Nicklass, A.; Palmieri, P.; Pitzer, R.; Schumann, U.; Stoll, H.; Stone, A. J.; Tarroni, R.; Thorsteinsson, T.

JP901903N